AGARD

ADVISORY GROUP FOR AEROSPACE RESEARCH & DEVELOPMENT

7 RUE ANCELLE 92200 NEUILLY SUR SEINE FRANCE

Paper Reprinted from
Conference Pre-Print No.139
on
Antennas for Avionics

NORTH ATLANTIC TREATY ORGANIZATION

ROLL PLANE ANALYSIS OF ON-AIRCRAFT ANTENNAS*

by
W.D. Burnside
R.J. Marhefka
C.L. Yu

The Ohio State University ElectroScience Laboratory
Department of Electrical Engineering
Columbus, Ohio 43212
28 June 1973

ABSTRACT

The roll plane radiation patterns of on-aircraft antennas are analyzed using high frequency solutions. This is a basic study of aircraft-antenna pattern performance in which the aircraft is modelled in its most basic form. The fuselage is assumed to be a perfectly conducting elliptic cylinder with the antennas mounted near the top or bottom. The wings are simulated by arbitrarily many sided flat plates and the engines by circular cylinders. The patterns in each case are verified by measured results taken on simple models as well as scale models of actual aircraft.

I. INTRODUCTION

This paper presents a basic theoretical study of roll-plane aircraft-antenna patterns for the UHF and microwave frequencies in which the antenna is mounted on the fuselage near the top or bottom. Since it is a study of general-type aircraft, the aircraft is modelled in its most basic form. The fuselage is assumed to be a perfectly conducting infinitely long elliptic cylinder. The wings and horizontal stabilizers are modelled by n-sided flat plates which lie in a plane that is parallel to the fuselage axis. The engines are approximated by circular cylinders.

The need for this type of solution is basically two-fold. First, there may be upwards to 200 antennas mounted on a single aircraft. If these antennas can be located on the aircraft at the design stage, then one can expect better performance in that optimum locations and necessary structural changes can be anticipated. Secondly, antenna systems are normally added or changed in the course of an aircraft's useful lifetime. Such relocation or addition of antennas has always required a great deal of engineering time and money.

Some of the first solutions used to compute on-aircraft antenna patterns were the modal solutions for infinitely long circular (Carter, P.S., 1943) and elliptical (Sinclair, G., 1951) cylinders. The fuselage was modelled by a cylinder whose cross-section approximated the fuselage cross-section at the antenna location. Arbitrary antennas were considered, and the antenna could be mounted on or above the fuselage. Results were quite adequate provided the aircraft structure was not illuminated too strongly. In fact, these solutions have provided the primary high frequency analysis to date. However, with the desire to improve system performance, versatility, and coverage the antenna pattern must be shaped for the desired application in such a way that it may actually illuminate the structure quite strongly. In many cases the system's performance is dependent on the pattern effects of the secondary contributors.

Another approach that has found great success at solving this type of problem is the Geometrical Theory of Diffraction (GTD). GTD is basically a high frequency solution (object large in terms of wavelength) which is divided into two basic problems; these being wedge or tip diffraction and curved surface diffraction. The only limitation of these solutions is that the source and various scattering centers be separated by at least a wavelength. In some cases even this requirement can be relaxed. Using this approach one applies a ray optics technique to determine the fields incident on the various scatterers. The fields diffracted are found using the GTD solutions in terms of rays which are summed with geometrical optics terms in the far zone. The scattered energy, which is analyzed in terms of rays, from a given structure tends to illuminate the other structures causing various higher-order scattered terms. Using the ray optics approach, one can trace out the various possible combinations of rays that interact between various scatterers and include only the dominant terms. Thus, one need only be concerned with the dominant scattering structures and neglect the secondary structures in the theoretical model. This makes the GTD approach ideal for a general high frequency study of on-aircraft antenna patterns.

II. WEDGE DIFFRACTION

The three dimensional wedge diffraction problem is pictured in Fig. 1. A source whose radiated $\bar{E}$ field is given by $\bar{E}^i(s)$ is located at point $s'(\rho',\phi',z')$. It can be an arbitrary electric or magnetic source causing plane, cylindrical, conical, or spherical wave incidence on the wedge tip. The diffracted vector field at point $s(\rho,\phi,z)$ can be written in terms of a dyadic diffraction coefficient. Kouyoumjian and Pathak (1970) have given a more rigorous basis for the GTD formulation and have shown that the diffracted fields may be written compactly if they are in terms of a ray-fixed coordinate system. The ray-fixed coordinate system is centered at the point of diffraction Q_E, (or points of diffraction in the case of plane wave incidence). Q_E is a unique point or points for a given source and observation point. The incident ray diffracts as a cone of rays such that $\beta_0 = \beta_0'$ (see Fig. 1).

For our purpose, it is more convenient to write the diffracted field in terms of the V_B function (Hutchins, D.L., 1967) as

(1)
$$\begin{bmatrix} E_\parallel^d(s) \\ E_\perp^d(s) \end{bmatrix} \sim \begin{bmatrix} -V_B^- & 0 \\ 0 & -V_B^+ \end{bmatrix} \begin{bmatrix} E_\parallel^i(Q_E) \\ E_\perp^i(Q_E) \end{bmatrix} \frac{\sqrt{L}\, e^{jkL}}{\sin \beta_0} \; A(s)\; e^{-jks}$$

where

$$V_B^\mp = V_B(L,\gamma^-,n) \mp V_B(L,\gamma^+,n) \; .$$

The time dependence factor $(e^{j\omega t})$ is suppressed throughout this paper. The minus sign (V_B^-) applies for the E-field component parallel to the edge and the plus sign (V_B^+) applies for the E-field component perpendicular to the edge. The angular relations are expressed by

$$\gamma = \gamma^\mp = \phi \mp \phi' \qquad \text{for} \quad 0 \leq \phi,\phi' \leq n\pi,$$

where the minus sign (γ^-) is associated with the incident field and the plus sign (γ^+) with the reflected field. The quantity $A(s)$ is a ray divergence factor given by (Pathak, P.K. etc., 1970)

$$A(s) = \begin{cases} \frac{1}{\sqrt{s}} & \text{plane, cylindrical } (s=\rho) \\ & \text{and conical wave incidence} \\[2mm] \sqrt{\frac{s'}{s(s'+s)}} & \text{spherical wave incidence} \end{cases}$$

and L is given by

$$L = \begin{cases} s\,\sin^2\beta_0 & \text{plane wave incidence} \\[2mm] \frac{\rho'\rho}{\rho+\rho'} & \text{cylindrical wave incidence} \\[2mm] \frac{s's\,\sin^2\beta_0}{s+s'} & \begin{array}{ll}\text{conical and} & \text{spherical wave} \\ \text{incidence.} & \text{incidence.}\end{array} \end{cases}$$

III. DIFFRACTION BY ELLIPTIC CYLINDER

The radiation from slots and monopoles mounted on smooth curved surfaces is pertinent to the design of flush-mounted antennas for aircraft and spacecraft. Recently, Pathak and Kouyoumjian (1972) have extended the GTD technique for plane wave diffraction by perfectly conducting convex surfaces to treat the radiation problem. This extension of GTD has been successfully applied to circular and elliptic cylinders, spheres, and spheroids (Burnside, W.D., 1972).

The GTD solution for the radiation by antennas mounted on convex surfaces employs the reciprocity theorem. Using this approach a plane wave field is assumed normally incident on a right circular cylinder. The antenna aperture field is, then, given by asymptotic solutions for exact expressions of the field on the cylinder surface. Employing the reciprocity theorem, one obtains the radiated field for that same antenna mounted on the cylinder. The geometrical optics solution is used to describe the radiated field in the lit region. The Fock approximation is used for the penumbra (transition) region; whereas in the deep shadow region, the GTD solution is applied. Using the GTD solution, a launch coefficient relates the antenna aperture field to the boundary layer surface waves which propagate around the surface along geodesic paths. Energy is continually diffracted by the surface wave in the tangent direction to the propagation path. This diffracted energy is given by a diffraction coefficient which is dependent on the surface geometry at the point of diffraction. The surface wave energy decays along the geodesic path in that energy is continually diffracted. This decay is expressed by an attenuation coefficient which is dependent on the surface geometry along the geodesic path.

The GTD solutions for infinitesimal slot and monopole antennas mounted on an elliptic cylinder as shown in Fig. 2 are given, neglecting torsional effects, by

A. Monopole case

Lit Region

(2) $\qquad \vec{E} = - \sin \theta_m \; \hat{\theta}_m \; F(\text{source})$

Transition Region

a) **Lit side**

(3) $\qquad \vec{E} = \hat{n} \left\{ (\sin \theta_m)^{\frac{1}{2}} \; e^{jk\ell} g^* \left[-\int \left(\frac{k}{2\rho_g^2(\ell)}\right)^{1/3} d\ell \right] \right\} \cdot F(\text{tangent})$

b) **Shadow side**

(4) $\qquad \vec{E} = \hat{n} \left\{ \frac{1}{2}\sqrt{\frac{d\psi_0}{d\psi}} \; e^{-jk\ell} \; g^* \left[\int \left(\frac{k}{2\rho_g^2(\ell)}\right)^{1/3} d\ell \right] \right\} \cdot F(\text{tangent})$

Deep Shadow

(5) $\qquad \vec{E} = \sum_j \hat{n}_j E_j^h F_j$ (tangent)

B. Slot case

Lit Region

(6) $\qquad \vec{E} = \left[(\hat{e}_1 \sin \beta - \hat{e}_2 \cos \beta) \cdot (\hat{b}'\hat{n}' + \hat{t}'\hat{b}') \right] \cdot F(\text{source})$

Transition region

    a) Lit side

(7) $\vec{E} = \left\{ \hat{n} \left[\frac{1}{2} e^{jk\ell} g^* \left(-\int \left(\frac{k}{2\rho_g^2(\ell)} \right)^{1/3} d\ell \right) \sin(\alpha_s + \beta) \right] + \right.$

$\qquad \left. \hat{b} \left[j/2 \, e^{jk\ell} \widetilde{g}^* \left(-\int \left(\frac{k}{2\rho_g^2(\ell)} \right)^{1/3} d\ell \right) \left(\frac{2}{k\rho_g} \right)^{1/3}_{\text{at source}} \cos(\alpha_s + \beta) \right] \right\} \cdot F(\text{tangent})$

    b) Shadow side

(8) $\vec{E} = \left\{ \hat{n} \; \frac{1}{2} \sqrt{\frac{d\psi_0}{d\psi}} \, e^{-jk\ell} \, g^* \left(\int \left(\frac{k}{2\rho_g^2(\ell)} \right)^{1/3} d\ell \right) \sin(\alpha_s - \beta) + \right.$

$\qquad \left. \hat{b} \left[-j/2 \sqrt{\frac{d\psi_0}{d\psi}} \, e^{-jk\ell} \, \widetilde{g}^* \left(\int \left(\frac{k}{2\rho_g^2(\ell)} \right)^{1/3} d\ell \right) \left(\frac{2}{k\rho g} \right)^{1/3}_{\text{at source}} \cos(\alpha_s - \beta) \right] \right\} \cdot F(\text{tangent})$

Deep Shadow Region

(9) $\vec{E} = \sum_j \left[\hat{n}_j E_j^h \sin(\alpha_s - \beta) + \hat{b}_j E_j^s \cos(\alpha_s - \beta) \right] F_j(\text{tangent})$

where

$\qquad E^h = \sqrt{\frac{d\psi_0}{d\psi}} \; \sum_{m=0}^{1} D_m^h L_m^h \, e^{-\int \gamma_m^h(\ell) d\ell}$

$\qquad E^s = \sqrt{\frac{d\psi_0}{d\psi}} \; \sum_{m=0}^{1} D_m^s L_m^s \, e^{-\int \gamma_m^s(\ell) d\ell} \qquad .$

The functions $g^*(\;)$ and $\widetilde{g}^*(\;)$ are the complex conjugates of the Fock function (Pathak, P.K., etc., 1972) for the hard and soft boundary conditions, respectively. The unit vectors $\hat{n}$ and $\hat{b}$ are, respectively, the normal and binormal to the geodesic curve at the diffraction (or tangent) point, and $F(\;)$ is simply a phase factor to refer the phase to the origin of the coordinate system. The term $\sqrt{d\psi_0/d\psi}$ is the spread factor, which is related to the spread of the geodesic paths. In this case, $\sqrt{d\psi_0/d\psi}$ is unity. The longitudinal and transverse radii of curvature are given, respectively, by ρ_g and ρ_t. Note that the superscripts h and s indicate the hard and soft boundary conditions. The launch coefficients are given by

$\qquad L_m^h = \left[\pi e^{j \frac{\pi}{12}} D_m^h \left(\frac{2}{k\rho_g} \right)^{1/3} A_i(-\bar{q}_m) \right]_{\text{at the source}}$

$\qquad L_m^s = \left[\pi e^{-j \frac{\pi}{12}} D_m^s \left(\frac{2}{k\rho_g} \right)^{2/3} A_i'(-q_m) \right]_{\text{at the source}}$

where D_m is defined in Table I. The subscript m refers to the mth mode of the boundary layer surface wave. Thus, γ_m is the propagation constant for the mth mode surface wave such that $\gamma_m = \alpha_m + jk$ where α_m is defined in Table I. The incremental arc length along the geodesic path is expressed by $d\ell$. The summation over "j" in the shadow region indicates that several terms can contribute in that region.

One must first find an efficient solution for the geodesic paths on the elliptic cylinder surface in order to analyze this problem successfully using GTD. A preferred coordinate system for the elliptic cylinder is illustrated in Fig. 3 and defined by

$\qquad\qquad x = d \cosh u \cos v = a_f \cos v$

(10) $\qquad y = d \sinh u \sin v = b_f \sin v$

$\qquad\qquad z = z$

where 2d is the distance between the foci of the ellipse. Note that for $u = u_f$, where $u_f = \tanh^{-1}(b_f/a_f)$ [a constant], the above equations define an elliptical surface for $0 \le v < 2\pi$. Thus, the elliptical surface shape is expressed by u_f, its size by d, and any point on the surface is defined by v.

Using the calculus of variations, the geodesic paths on an elliptical surface are given by

$$z = \frac{c}{\sqrt{1-c^2}} \int_{v_i}^{v_f} \sqrt{a_f^2 \sin^2 v + b_f^2 \cos^2 v} \, dv \quad .$$

Note that v_i and v_f are, respectively, the initial and final values of v along a given geodesic path. If one defines the geodesic starting direction by the angle (α_s) as shown in Fig. 2, then $C = -\cos \alpha_s$. The advantage of this geodesic solution lies in the fact that the integral can be quickly evaluated using numerical techniques. The important parameters of this problem are listed below:

$$z = \frac{-\cos \alpha_s}{|\sin \alpha_s|} \int_{v_i}^{v_f} \sqrt{a_f^2 \sin^2 v + b_f^2 \cos^2 v} \, dv \qquad \text{(geodesic equation)}$$

$$\ell = \frac{1}{|\sin \alpha_s|} \int_{v_i}^{v_f} \sqrt{a_f^2 \sin^2 v + b_f^2 \cos^2 v} \, dv \qquad \text{(arc length)}$$

$$\left. \begin{array}{l} \hat{e}_1 = \dfrac{-a_f \sin v \, \hat{x} + b_f \cos v \, \hat{y}}{\sqrt{a_f^2 \sin^2 v + b_f^2 \cos^2 v}} \\[2em] \hat{e}_2 = \hat{z} \end{array} \right\} \qquad \text{(curvalinear coordinates)}$$

$$\hat{t} = \sin \alpha_s \, \hat{e}_1 - \cos \alpha_s \hat{e}_2 \qquad \text{(unit tangent vector)}$$

$$\hat{n} = \frac{b_f \cos v \, \hat{x} + a_f \sin v \, \hat{y}}{\sqrt{a_f^2 \sin^2 v + b_f^2 \cos^2 v}} \qquad \text{(unit normal vector)}$$

$$\hat{b} = \hat{t} \times \hat{n} = + \cos \alpha_s \, \hat{e}_1 + \sin \alpha_s \, \hat{e}_2 \qquad \text{(unit binormal vector)}$$

$$\rho_g = \frac{(a_f^2 \sin^2 v + b_f^2 \cos^2 v)^{3/2}}{a_f \, b_f \sin^2 \alpha_s} \qquad \begin{array}{l}\text{(longitudinal radius of}\\ \text{curvature)}\end{array}$$

Using the above relations, one can employ Eqs. (2-9) to determine the total radiated fields.

The principal plane radiation patterns (which correspond to roll plane patterns in the aircraft case) are shown in Fig. 4 for a circumferential slot, axial slot, and monopole mounted on a two wavelength radius circular cylinder. These patterns compare very favorably with the modal solutions (Sinclair, G., 1951) as shown in the same figures. The principal plane radiation patterns are shown in Fig. 5 for the same antennas mounted on an elliptic cylinder.

IV. NEAR FIELD SCATTERING BY A FINITE PLATE

The near field scattering by a finite flat plate is a relatively new topic at higher frequencies where the plate is large in terms of the wavelength. The solution presented here is a practical application of the three-dimensional wedge diffraction theory given earlier. The source is defined by its location and far-field pattern. The far-field pattern of the source is appropriate in that the plate is located at least $2D^2/\lambda$ away from the source where D is the maximum dimension of the source. The finite flat plate is simply specified by location of its n corners.

It is known that for a given scatter direction there is only one point along an infinitely long straight edge at which the diffracted field can emanate for a near zone source. Thus, this point must be found for each of the n edges that describe the flat plate. There are many ways of finding this diffraction point, one of which is described here. Since it is known that $\beta_o = \beta_o'$ (see Fig. 1), it is obvious that

$$(11) \qquad \hat{e}_m \cdot \hat{I} = \hat{e}_m \cdot \hat{d}$$

where $\hat{e}_m$, $\hat{I}$, and $\hat{d}$ are, respectively, the mth edge unit vector, incident direction unit vector, and diffraction direction unit vector. Since the scatter direction is known (θ_s, ϕ_s), the value of $\hat{e}_m \cdot \hat{d} = c_m$ is easily computed for each edge. One need only search along the edge to find the point where $\hat{e}_m \cdot \hat{I} = c_m$.

Once the diffraction point is located, one must find the diffracted field value from the mth edge. The far field pattern of the source can be written as

(12) $\vec{E}_s(\theta,\phi) = [\hat{\theta}F(\theta,\phi) + \hat{\phi}G(\theta,\phi)]\dfrac{e^{-jks'}}{s'} = \vec{R}(\theta,\phi)\dfrac{e^{-jks'}}{s'}$

where s' is the range from the source to the field point. Using the geometry illustrated in Fig. 1 and applying the results presented earlier one finds that

(13) $\begin{bmatrix} R_{\parallel}^d \\ R_{\perp}^d \end{bmatrix} = \begin{bmatrix} -V_B^- & 0 \\ 0 & -V_B^+ \end{bmatrix} \begin{bmatrix} R_{\parallel}^i \\ R_{\perp}^i \end{bmatrix} e^{-j[k(s'-\gamma)-k_\rho\rho]}$

where

$R_{\parallel}^i = \vec{R}(\theta_i,\phi_i) \cdot \hat{\beta}_0'$

$R_{\perp}^i = \vec{R}(\theta_i,\phi_i) \cdot \hat{\phi}_0$

$k_\rho\rho = ks' \sin^2\beta_0$

$\gamma = x_{dp} \sin\theta_s \cos\phi_s + y_{dp} \sin\theta_s \sin\phi_s + z_{dp} \cos\theta_s$

$V_B^{\pm} = V_B(k_\rho\rho,\phi-\phi',2) \mp V_B(k_\rho\rho,\phi+\phi',2)$

$\hat{\phi}_0 = \hat{I} \times \hat{\beta}_0'$.

The coordinates (x_{dp}, y_{dp}, z_{dp}) define the point of diffraction.

Once these terms are determined the total diffracted field in ray form from a general mth edge is given by

(14) $\vec{R}_m^d(\theta_s,\phi_s) = R_{\parallel}^d \hat{\beta}_0 + R_{\perp}^d \hat{\phi}$,

where $\hat{\phi} = \hat{d} \times \hat{\beta}_0$. Using the superposition principle the total singly diffracted field in ray form by the n edges of the flat plate is given using Eq. (14) by

(15) $\vec{R}^d(\theta_s,\phi_s) = \sum_{m=1}^{n} \vec{R}_m^d(\theta_s,\phi_s)$.

The first step in calculating the reflected field is to find the location of the image source, which is uniquely determined once the plane of the flat plate is defined relative to the source location. In fact, the image is located along a line which is orthogonal to the plate and positioned an equal distance on the opposite side of the plate.

With the image position known, one needs to determine if the reflected field contributes to the total scattered field using the geometrical optics approach. If the reflected field is a contributor, the ray from the image source in the scatter direction (θ_s,ϕ_s) must pass through the finite plate limits. Thus, one must find the location of the intersection point of this ray and the plane containing the flat plate. This can easily be accomplished using vector analysis. One can, then, predict within certain limits whether this intersection point falls within the bounds of the finite flat plate.

If reflections do occur, the reflected field from the image source can be written in ray form as

(16) $\vec{R}^r(\theta_s,\phi_s) = [\hat{\theta}^rF^r(\theta_s,\phi_s)+\hat{\phi}^rG^r(\theta_s,\phi_s)] \cdot e^{jk[x_i \sin\theta_s \cos\phi_s + y_i \sin\theta_s \sin\phi_s + z_i \cos\theta_s]}$

where $\hat{\theta}^r$ and $\hat{\phi}^r$ are related to the image source coordinate system with the image location defined by (x_i,y_i,z_i). The functions $[F^r(\theta_s,\phi_s)$ and $G^r(\theta_s,\phi_s)]$ are found by employing the boundary conditions on the perfectly conducting flat plate. The total scattered field from the flat plate is, then, given by

(17) $\vec{R}^s(\theta_s,\phi_s) = \vec{R}^d(\theta_s,\phi_s) + \vec{R}^r(\theta_s,\phi_s)$.

In order to illustrate the versatility of this solution, it is used to approximate the scattering effect of a disc. This is done by computing the pattern of a monopole mounted on plates with increasingly many sides. In Fig. 6 the calculated results for plates with 4, and 6 sides are illustrated and compared with the measured result for the circular disk (Lopez, A.R., 1966). Note that as the number of sides is increased the closer the computed and measured results agree. Note also the agreement between measured and calculated patterns of a $\lambda/4$ dipole mounted above a square plate as illustrated in Fig. 7.

Even though the above results show good agreement one must realize the inherent approximations in this solution. It is based on edge diffraction with just singly diffracted edge rays being considered. Thus, it has been assumed that the plate is large in terms of the wavelength such that double diffraction is normally negligible. However, neglecting double diffraction may cause some error especially when the pattern is computed in the plane of the flat plate. Secondly, a diffraction term from each of the corners should be included, but it is not available in practical form at present. Nevertheless, the latter has little effect on the overall pattern except when a diffraction point (or points) approaches a corner. In these two cases our solution can be somewhat in error although only small angular regions are involved.

V. ROLL PLANE ANALYSIS

The basic aircraft to be analyzed in this study is composed of flat plates and cylinders. It is assumed that the source is mounted on the fuselage and restricted to the regions near the top or bottom of the aircraft. Arbitrary antennas can be considered simply by integrating these solutions for infinitesimal antennas over the equivalent aperture currents.

The lower frequency limit of these solutions is dictated by the ray optics format which requires that the various scattering centers be no closer than approximately a wavelength with the overall aircraft being large in terms of the wavelength. The upper frequency limit is dictated by the accuracy to which the model represents the actual aircraft considered.

The two-dimensional problem is considered initially in order to develop the necessary techniques to attack the much more difficult three-dimensional roll plane problem (Marhefka, R.J., 1971). The geometry of the two-dimensional problem is illustrated in Fig. 8 with and without the engines included. The fuselage and engines are assumed circular in cross-section and mounted symmetrically about the finite wing. Since wedge diffraction is applied to handle the finite length wing, the radiated field must be described in terms of rays. However, one of the nicer features of the GTD approach is that other solutions such as modal solutions can be cast into a ray form and then applied to a diffraction problem. Consequently, it was found that the modal solution (Sinclair, G., 1951) for an arbitrary antenna mounted on an infinite circular cylinder was satisfactory for treating the antenna mounted on the circular fuselage. In fact, this solution has been applied in past years as the sole solution for high frequency on-aircraft antenna analyses.

The radiation patterns for an axial slot are shown in Fig. 8a on a model without engines. The slot used for the measured patterns is simply an open-ended X-band waveguide. These solutions compare very favorably with measured results taken on a simulated two-dimensional aircraft model. The radiation patterns for the same configuration with the engines added are illustrated in Fig. 8b. Again very good agreement is obtained between our calculated and measured results. These results indicate that the scattering from the engines has little effect on the overall pattern except near $\phi \sim 90^\circ$ and $\phi \sim 270^\circ$. The same conclusion is true for the monopole and circumferential slot which were analyzed and measured although not shown here.

Since the roll plane cuts orthogonally across the fuselage, one should expect the fuselage cross-section to have a strong effect on the roll plane pattern. On the other hand, an aircraft fuselage is normally long and slender, such that its finite length effects are generally secondary. Consequently, the infinite elliptic cylinder representation of the fuselage for roll plane calculations appears to be a reasonable approximation in most cases. Since the antenna can be arbitrarily positioned on the fuselage with respect to the wings, one must consider the width of the wing as well as its length in order to obtain a practical analytic model. In order to accomplish this, the near field flat plate scattering solution is adapted to this new model such as illustrated in Fig. 9. Note that each wing can be located arbitrarily with any number of edges provided only that the wings are flat and horizontal.

Our model, now, consists of an infinitely long elliptic cylinder fuselage to which finite flat wings are attached. The various configurations analyzed are shown in Fig. 10 looking from the front of the aircraft with the antenna mounted in each case above the wings for the models illustrated. Using these models, one should be able to analyze a wide variety of aircraft shapes. This is verified by a comparison of results taken on actual aircraft scale models and presented later.

Let us first find the effective source location for the reflected field. Recall that in our flat plate result the source was imaged and the reflected field added to the total solution provided the image ray passed through the finite flat plate (wing) limits. So one must initially determine the effective source position and then the reflected field. With the source mounted on an infinitely long elliptic cylinder, the surface rays from the source propagate around the cylinder along geodesic paths, from which energy is continually diffracted tangentially. Now let us assume that the source does not illuminate the right wing directly (as illustrated in Fig. 9a) and proceed to determine the unique geodesic path that diffracts energy from a known tangent point which is then reflected off the wing in the desired radiation (or scatter) direction.

The effective source position for reflections from the right wing in terms of the radiation direction (θ_s, ϕ_s) is given by

$$
\begin{aligned}
x_e &= a_f \cos v_e \\
y_e &= b_f \sin v_e \\
z_e &= \cot \theta_s \int_{v_{so}}^{v_e} \sqrt{a_f^2 \sin^2 v + b_f^2 \cos^2 v}\, dv + z_{so}
\end{aligned}
\tag{18}
$$

where $v_e = \tan^{-1}(b_f/a_f \cot \phi_s)$. These coordinates can, then, be used in the flat plate problem as the effective source location. Note that as the desired radiation direction is varied the effective source location changes. In addition, if the source directly illuminates the wing for a given reflection term then the effective source location is simply the actual source location (u_f, v_{so}, z_{so}). A result similar to Eq. (18) can be found for the reflections from the left wing. Finally, the actual source field value used to compute the reflected term is determined from the GTD solutions of Section III.

Using a similar technique the effective source locations for the diffracted field components may be found. Our flat plate solution uses a search technique to find the diffraction point by computing the diffraction angles at selected test points along a given edge. Once a test point (x_d, y_d, z_d) is specified along the edge one can find the effective source location (x_e, y_e, z_e) using the geometry illustrated in Fig. 9b. Again it is assumed that the source does not directly illuminate the test point. One finds that the effective source is given by

$$x_e = \frac{a_f^2 b_f^2 x_d + a_f^2 y_d \sqrt{a_f^2 y_d^2 + b_f^2 x_d^2 - a_f^2 b_f^2}}{(a_f^2 y_d^2 + b_f^2 x_d^2)}$$

$$(19) \qquad y_e = \frac{a_f^2 b_f^2 y_d - b_f^2 x_d \sqrt{a_f^2 y_d^2 + b_f^2 x_d^2 - a_f^2 b_f^2}}{(a_f^2 y_d^2 + b_f^2 x_d^2)}$$

$$z_e = \frac{b_f x_e z_d I_v + a_f z_{so}(y_d - y_e) I_v'}{b_f x_e I_v + a_f(y_d - y_e) I_v'}$$

where

$$I_v = \int_{v_{so}}^{v_e} \sqrt{a_f^2 \sin^2 v + b_f^2 \cos^2 v} \; dv,$$

$$I_v' = \sqrt{a_f^2 \sin^2 v_e + b_f^2 \cos^2 v_e}, \quad \text{and} \quad v_e = \tan^{-1}\left(\frac{y_e/b_f}{x_e/a_f}\right).$$

Given the effective source location for the chosen test point, the search technique is applied to find the actual diffraction point along a given edge. Note that once the actual diffraction point is determined, the effective source of the diffracted field is specified by Eq. (19), and the source field value is, again, computed using the GTD solutions.

The total field is found by summing the directly radiated field with the scattered fields from the wings using the superposition principle. Several different configurations have been studied using this solution and compared with measured results. The patterns illustrated in Fig. 11 are based on a circular fuselage with the wings mounted in the central location. The roll plane pattern for $\lambda/4$ monopole is shown in Fig. 11a, with the antenna mounted directly above the wings. The pattern is shown in Fig. 11b for an axial slot mounted on the fuselage over the back limit of the wing. In Fig. 11c the pattern is shown for a circumferential slot mounted over the wings but rotated 45° from the straight up direction as considered in Fig. 11a. The patterns for a $\lambda/4$ monopole mounted on a circular fuselage wing above and below the central location are illustrated in Fig. 12. In Fig. 13 the roll plane patterns are illustrated for each of the three basic antennas mounted on an elliptic fuselage with the wings centrally attached. The patterns illustrated in Fig. 14 are for an axial slot mounted on an elliptic fuselage with the wings above and below the central position. Good agreement is obtained between the calculated and measured results in each case. The slight deviations are attributed primarily to the assumptions made in solving for the flat plate scattered field.

VI. CONCLUSIONS

The solutions that have been presented here provide a high-speed analytic tool for determining the type and location of antennas based on their roll plane performance. These programs typically compute a pattern in 30 seconds or less on a CDC 6600 digital computer. A 16 mm film has been developed which illustrates the advantages of a numerical solution for computing patterns for antennas on aircraft and is available upon request.

An additional feature of these solutions, which can be very important in certain critical cases, is that one can trace out the dominant pattern terms as they are scattered by the various parts of the aircraft structure. In this way one can quickly ascertain which structural scatterers are distorting the pattern in a critical region. This gives one the option of taking corrective action by changing the structure or by properly placing absorber. So these solutions not only provide fast pattern computations, but they also provide the antenna designer with a means of analytically considering several alternatives to improve the antenna's performance.

Each of the solutions developed have been verified by experimental results taken on a structure which approximates our analytic model. However, these results do not verify the general validity of our analytic model in representing an actual aircraft. There are no roll plane patterns published in the literature to our knowledge that would be suitable for our comparison. We appreciate the efforts of NASA personnel who measured the patterns of a $\lambda/4$ monopole mounted on an accurately scaled model of a KC-135 (Boeing 707); as well as, the effort of NADC personnel who measured two patterns on a scale model of a F-4 aircraft. The results are illustrated in Figs. 15 and 16 and the agreement in each case is very encouraging.

REFERENCES

Burnside, W.D., "Analysis of On-Aircraft Antenna Patterns," Report 3390-1, August 1972, The Ohio State University ElectroScience Laboratory, Department of Electrical Engineering; prepared under Contract N62269-72-C-0354 for Naval Air Development Center.

Carter, P.S., "Antenna Arrays Around Cylinders," Proc. IRE, Vol. 31, December, 1943, pp. 671-693.

Hutchins, D.L., "Asymptotic Series Describing the Diffraction of a Plane Wave by a Two-Dimensional Wedge of Arbitrary Angle," Ph.D. Dissertation, The Ohio State University, Department of Electrical Engineering, (1967).

Lopez, A.R., "The Geometrical Theory of Diffraction Applied to Antenna Pattern and Impedance Calculations," IEEE Transactions on Antennas and Propagation, Vol. AP-14, No. 1, (January 1966), p. 40.

Marhefka, R.J., "Roll Plane Analysis of On-Aircraft Antennas," Report 3188-1, December 1971, The Ohio State University ElectroScience Laboratory, Department of Electrical Engineering; prepared under Contract N62269-71-C-0296 for Naval Air Development Center.

Pathak, P.H. and Kouyoumjian, R.G., "The Dyadic Diffraction Coefficients for a Perfectly Conducting Wedge," Scientific Report No. 5, Report 2183-4, 5 June 1970, The Ohio State University ElectroScience Laboratory, Department of Electrical Engineering; prepared under Contract AF19(628)-5929 for Air Force Cambridge Research Laboratories.

Pathak, P.H. and Kouyoumjian, R.G., "The Radiation from Apertures in Curved Surfaces," Report 3001-2, December 1972, The Ohio State University ElectroScience Laboratory, Department of Electrical Engineering; prepared under Grant NGR 36-008-144 for National Aeronautics and Space Administration.

Sinclair, G., "The Patterns of Antennas Located Near Cylinders of Elliptical Cross Section," Proc. IRE, Vol. 39, No. 6, June 1951.

TABLE I
GENERALIZED DIFFRACTION COEFFICIENTS AND ATTENUATION CONSTANTS

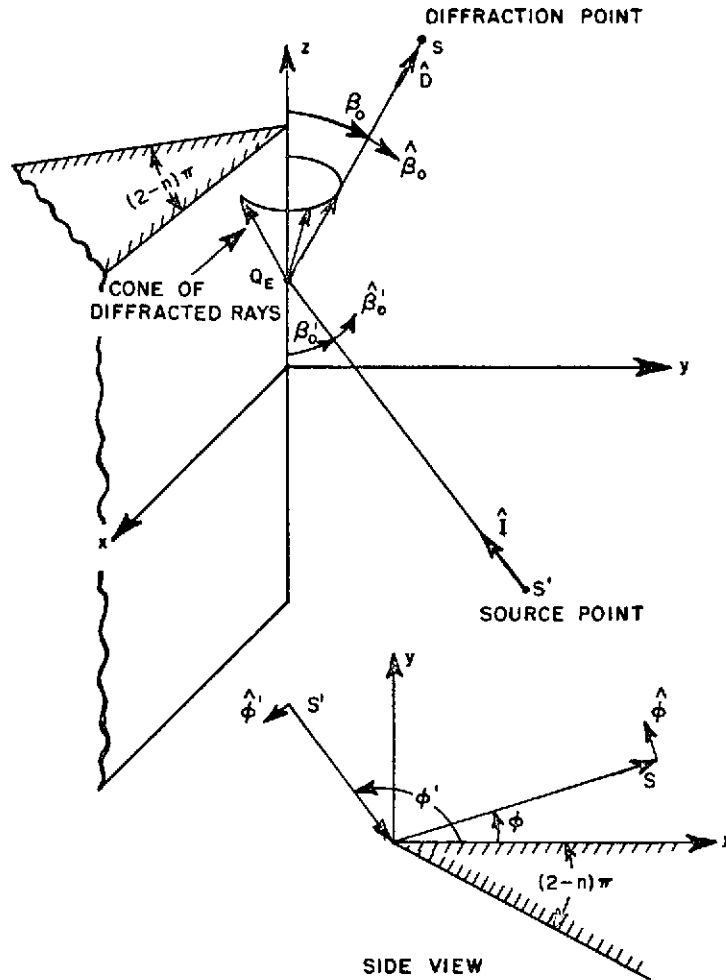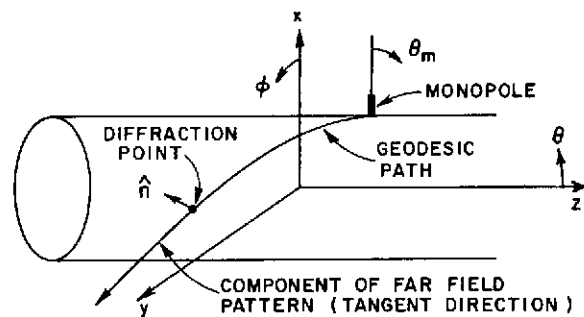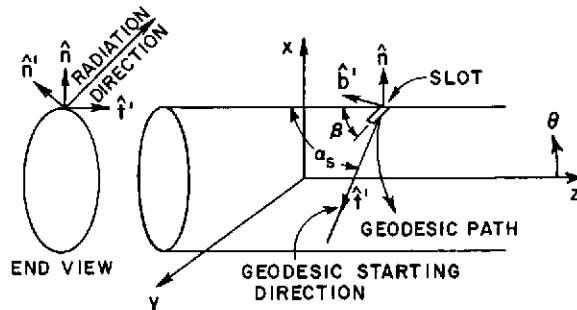| Surface	Square of Diffraction Coefficient D_m^2 = (Column A) · (Column B)		Attenuation Constant α_m = (Column C) · (Column D)	
	A. Keller's Result	B. Correction Terms	C. Keller's Result	D. Correction Terms
Soft Acoustic and Soft EM	$\dfrac{\tau^{-1/2} z^{-5/6} \rho_g^{1/3} e^{-j\pi/12}}{k^{1/6} Ai'(-q_m)^2}$	$1 + \left(\dfrac{2}{k\rho_g}\right)^{2/3} q_m \left(\dfrac{1}{15} + \dfrac{\rho_g}{4\rho_{tn}} + \dfrac{\rho_g\bar{\rho}_g}{180}\right) e^{-j\pi/3}$	$\dfrac{q_m}{\rho_g} e^{j\pi/6}\left(\dfrac{k\rho_g}{2}\right)^{1/3}$	$1 + \left(\dfrac{2}{k\rho_g}\right)^{2/3} q_m\left(\dfrac{1}{60} - \dfrac{2}{45}\rho_g\bar{\rho}_g + \dfrac{4}{135}\bar{\rho}_g^2\right)e^{-j\pi/3}$
Hard Acoustic		$1 + \left(\dfrac{2}{k\rho_g}\right)^{2/3}\left(\bar{q}_m\left(\dfrac{1}{30} + \dfrac{\rho_g}{4\rho_{tn}} + \dfrac{\rho_g\bar{\rho}_g}{180}\right) - \dfrac{1}{\bar{q}_m}\left(\dfrac{1}{10} + \dfrac{\rho_g}{4\rho_{tn}} - \dfrac{\rho_g\bar{\rho}_g}{60}\right)\right)e^{-j\pi/3}$		$1 + \left(\dfrac{2}{k\rho_g}\right)^{2/3}\left(\bar{q}_m \dfrac{1}{60} - \dfrac{2}{45}\rho_g\bar{\rho}_g + \dfrac{4}{135}\bar{\rho}_g^2\right) + \dfrac{1}{\bar{q}_m}\left(\dfrac{1}{10} + \dfrac{\rho_g}{4\rho_{tn}} - \dfrac{\rho_g\bar{\rho}_g}{60} + \dfrac{\bar{\rho}_g^2}{90}\right)\right)e^{-j\pi/3}$
Hard EM	$\dfrac{\tau^{-1/2} z^{-5/6} \rho_g^{1/3} e^{-j\pi/12}}{k^{1/6} \bar{q}_m (Ai(-\bar{q}_m))^2}$	$1 + \left(\dfrac{2}{k\rho_g}\right)^{2/3}\left(\bar{q}_m\left(\dfrac{1}{30} + \dfrac{\rho_g}{4\rho_{tn}} + \dfrac{\rho_g\bar{\rho}_g}{180}\right) - \dfrac{1}{\bar{q}_m}\left(\dfrac{1}{10} - \dfrac{\rho_g}{4\rho_{tn}} - \dfrac{\rho_g\bar{\rho}_g}{60}\right)\right)e^{-j\pi/3}$	$\dfrac{\bar{q}_m}{\rho_g} e^{j\pi/6}\left(\dfrac{k\rho_g}{2}\right)^{1/3}$	$1 + \left(\dfrac{2}{k\rho_g}\right)^{2/3}\left(\bar{q}_m\left(\dfrac{1}{60} - \dfrac{2}{45}\rho_g\bar{\rho}_g + \dfrac{4}{135}\bar{\rho}_g^2\right) + \dfrac{1}{\bar{q}_m}\left(\dfrac{1}{10} - \dfrac{\rho_g}{4\rho_{tn}} - \dfrac{\rho_g\bar{\rho}_g}{60} + \dfrac{\bar{\rho}_g^2}{90}\right)\right)e^{-j\pi/3}$

DIFFRACTION POINT

CONE OF
DIFFRACTED RAYS

Q_E

$(2-n)\pi$

β_0

$\hat{D}$

$\hat{\beta}_0$

$\hat{\beta}_0^i$

β_0

$\hat{I}$

S'

SOURCE POINT

SIDE VIEW

$\hat{\phi}^i$ S'

ϕ^i

ϕ

$\hat{\phi}$

S

$(2-n)\pi$

Fig. 1. Geometry for three-dimensional wedge diffraction problem.

θ_m

MONOPOLE

ϕ

DIFFRACTION
POINT

$\hat{n}$

GEODESIC
PATH

θ

COMPONENT OF FAR FIELD
PATTERN (TANGENT DIRECTION)

(a) GEOMETRY OF MONOPOLE PROBLEM

$\hat{n}^i$ $\hat{n}$

RADIATION
DIRECTION

$\hat{t}^i$

$\hat{b}^i$

SLOT

β^i

a_s

θ

$\hat{t}^i$

GEODESIC PATH

END VIEW

GEODESIC STARTING
DIRECTION

(b) GEOMETRY OF SLOT PROBLEM

Fig. 2. Geometry of antennas mounted on an infinitely long
elliptic cylinder.
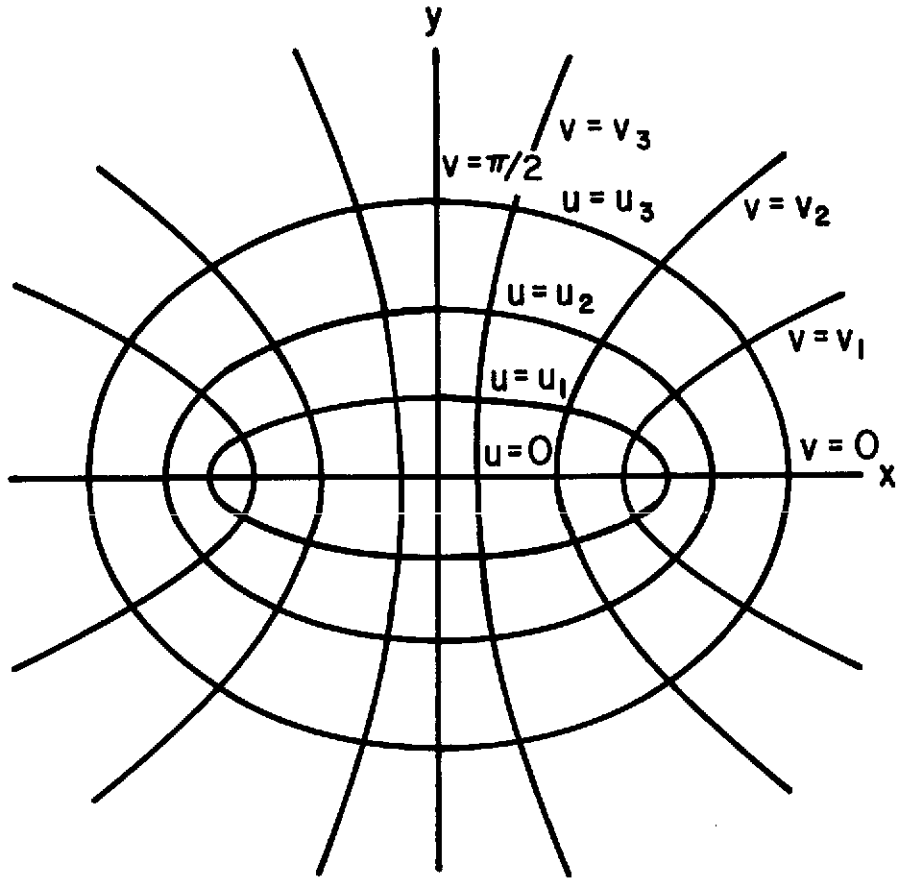
Fig. 3. Diagram showing the elliptic cylinder coordinate system.
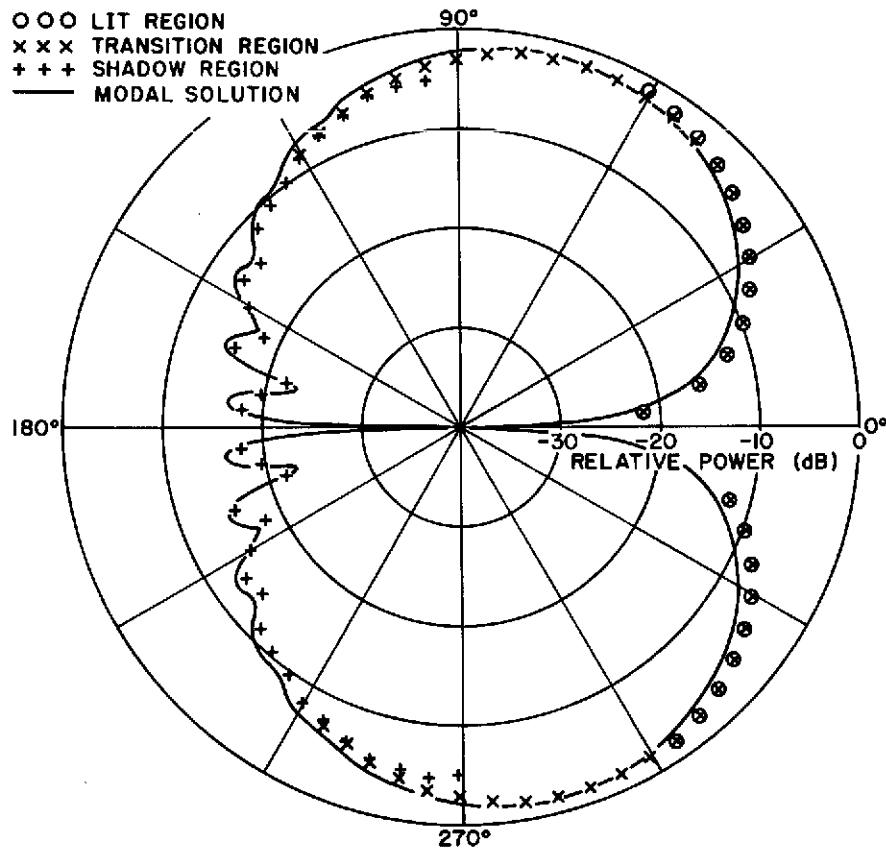
Fig. 4a. Principal plane pattern of a monopole mounted on a 2λ
radius circular cylinder.
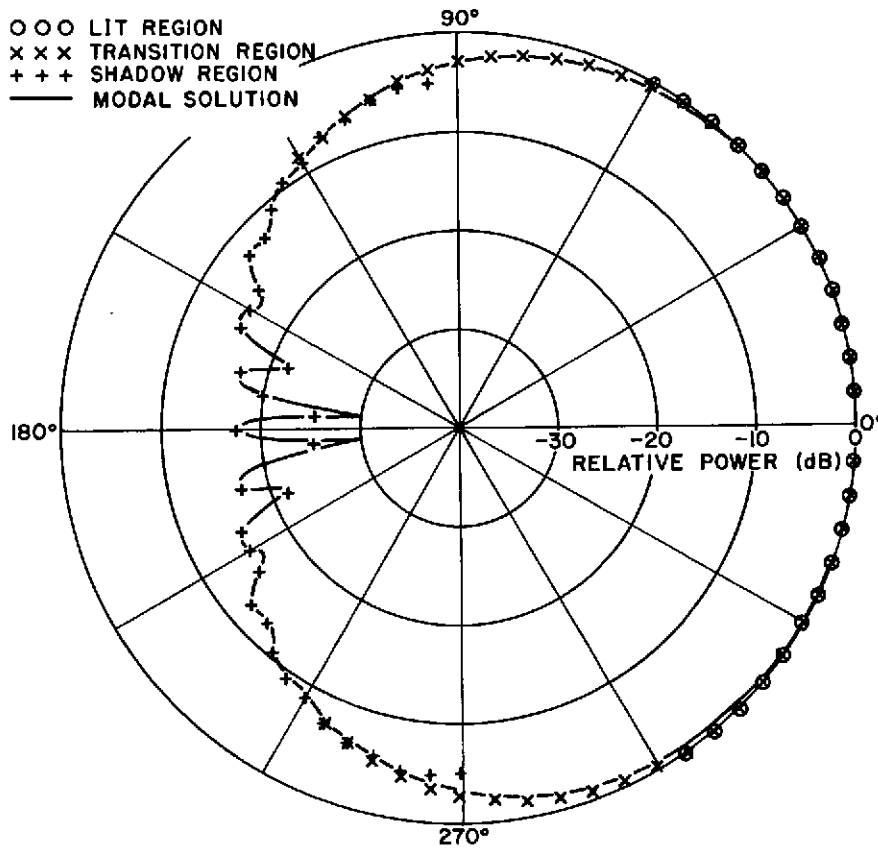
O O O LIT REGION
X X X TRANSITION REGION
+ + + SHADOW REGION
——— MODAL SOLUTION

90°

180°

-30   -20   -10   0°
RELATIVE POWER (dB)

270°

Fig. 4b. Principal plane pattern of an axial slot mounted on a 2λ
radius circular cylinder.

O O O LIT REGION
X X X TRANSITION REGION
+ + + SHADOW REGION
——— MODAL SOLUTION

90°

180°

-30   -20   -10   0°
RELATIVE POWER (dB)

270°

Fig. 4c. Principal plane pattern of a circumferential slot mounted
on a 2λ radius circular cylinder.

O O O LIT REGION
x x x TRANSITION REGION
+ + + SHADOW REGION

Fig. 5a. Principal plane pattern of a monopole mounted on an elliptic
cylinder with a_f = 4λ and b_f = 2λ.

O O O LIT REGION
x x x TRANSITION REGION
+ + + SHADOW REGION

Fig. 5b. Principal plane pattern of an axial slot mounted on an
elliptic cylinder with a_f = 4λ and b_f = 2λ.

7

O O O LIT REGION
× × × TRANSITION REGION
+ + + SHADOW REGION
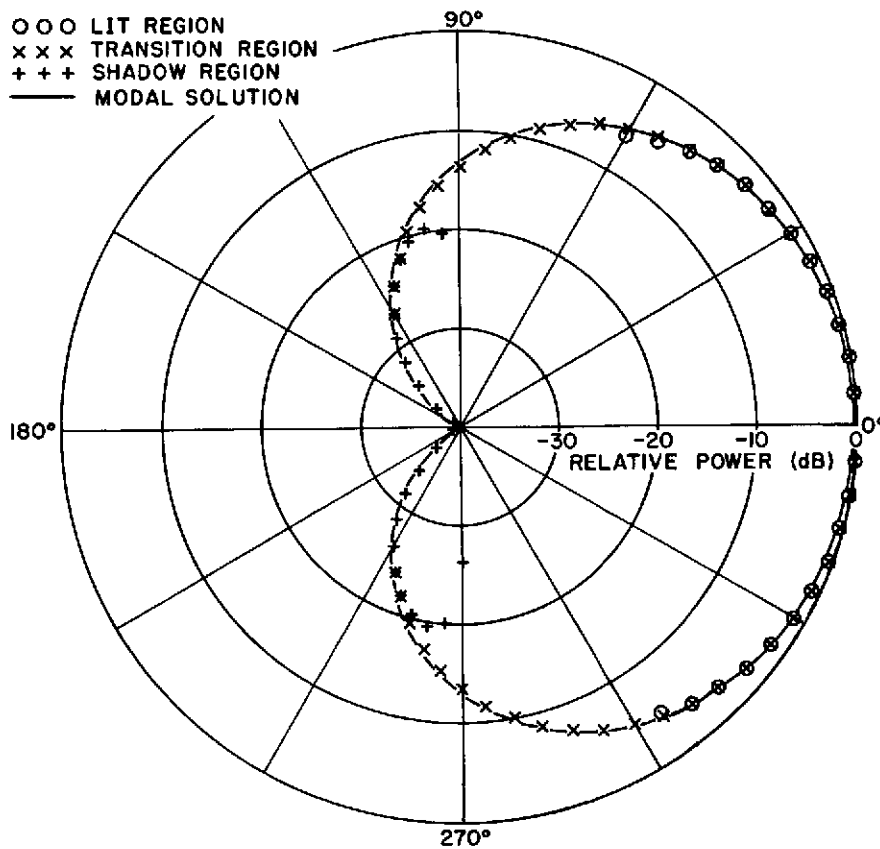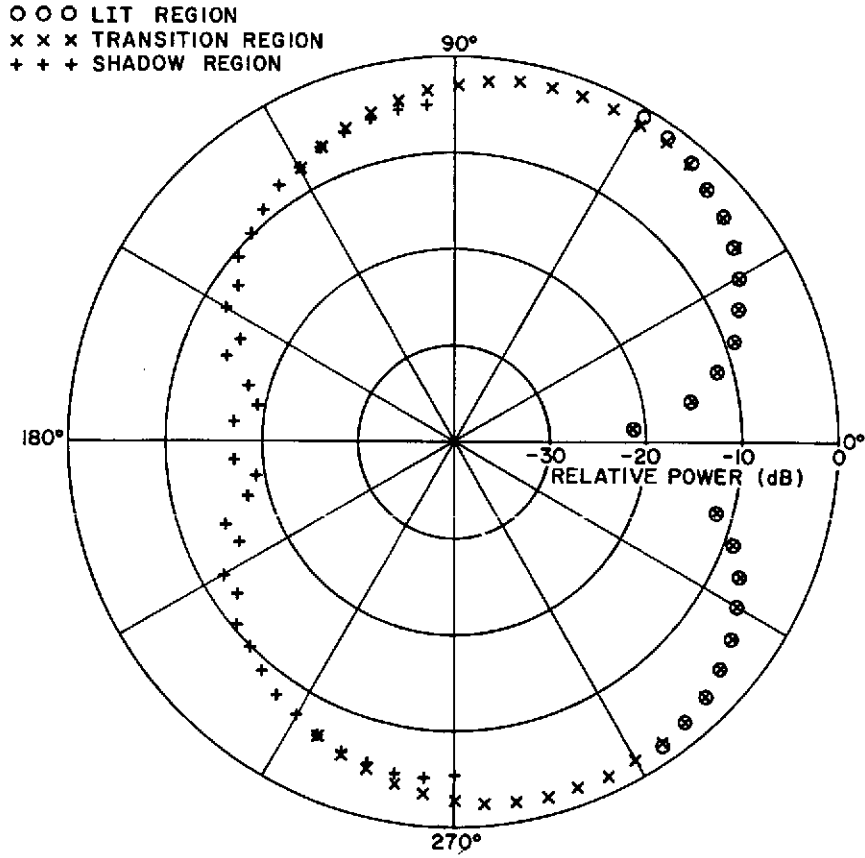
Fig. 5c. Principal plane pattern of a circumferential slot mounted on an elliptic cylinder with $a_f = 4\lambda$ and $b_f = 2\lambda$.

————— MEASURED ON CIRCULAR Gnd PLANE
— — — — 4 SIDED FLAT PLATE
•••••••• 6 SIDED FLAT PLATE
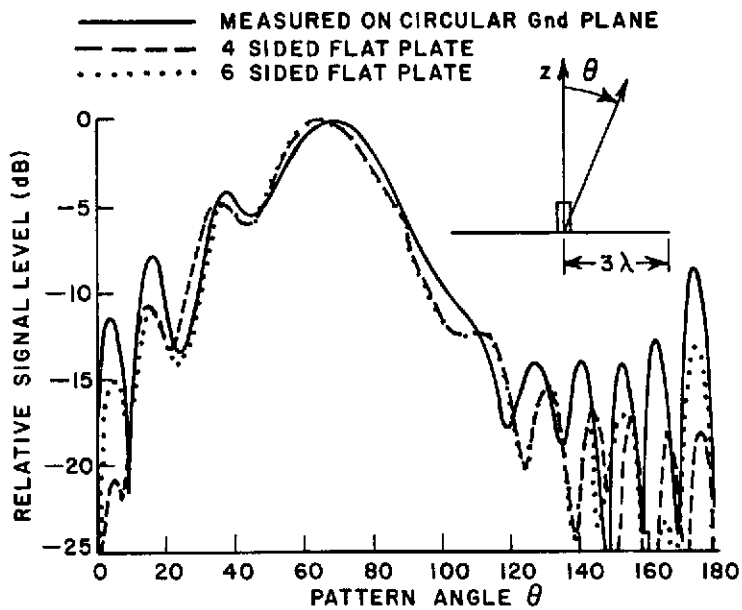
Fig. 6. Radiation pattern of a stub on a circular ground plane.
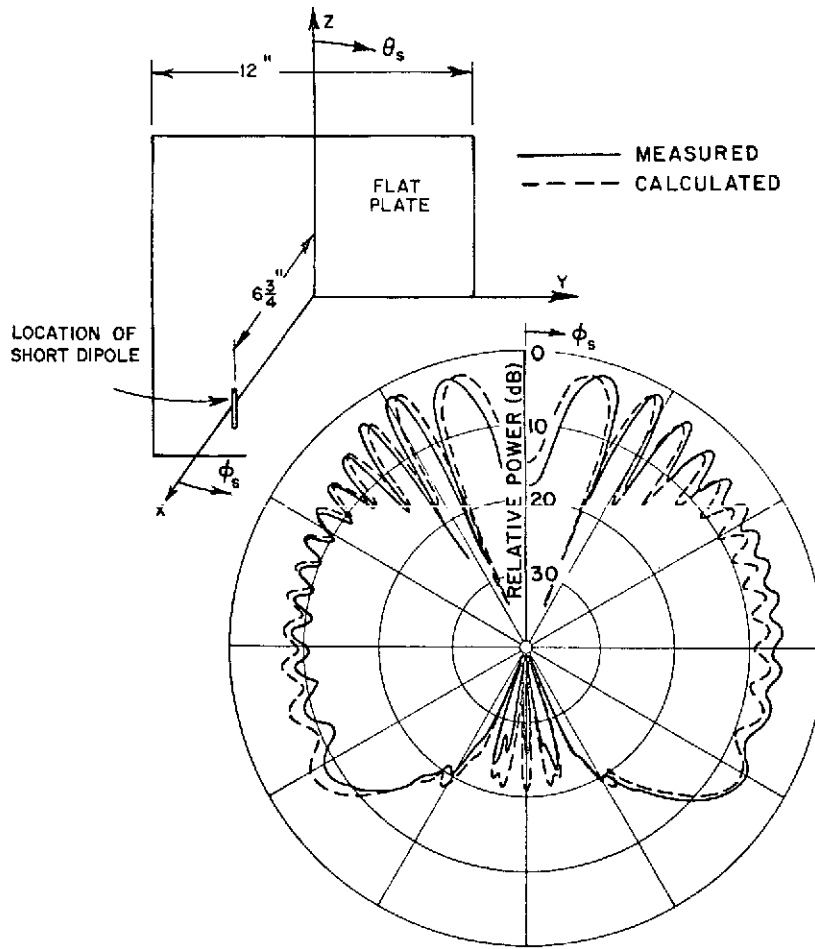
Fig. 7. E_ϕ radiation pattern for a small dipole mounted above a rectangular plate for $\theta_s = 90^0$ and $0^0 < \phi_s \leq 360^0$ at f = 10.43 GHz.
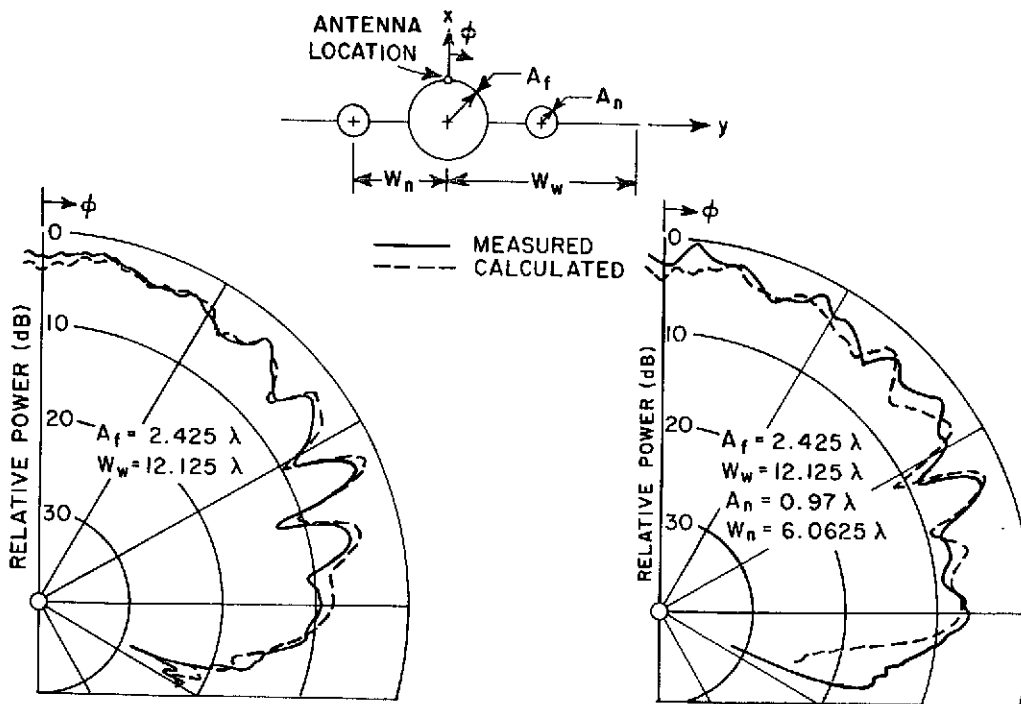
Fig. 8a. E_ϕ radiation pattern for an axial slot on a fuselage with finite length wing at f = 11.45 GHz.

Fig. 8b. E_ϕ radiation pattern for an axial slot on a fuselage with engine and finite length wing at f = 11.45 GHz.
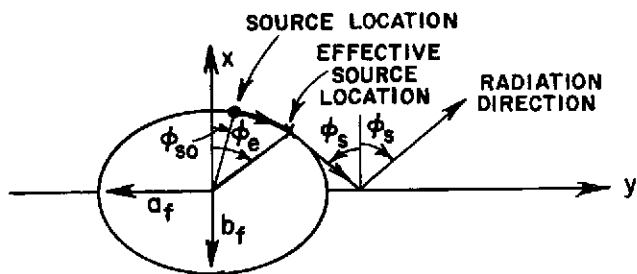
Fig. 9a. Reflection problem in x-y plane.
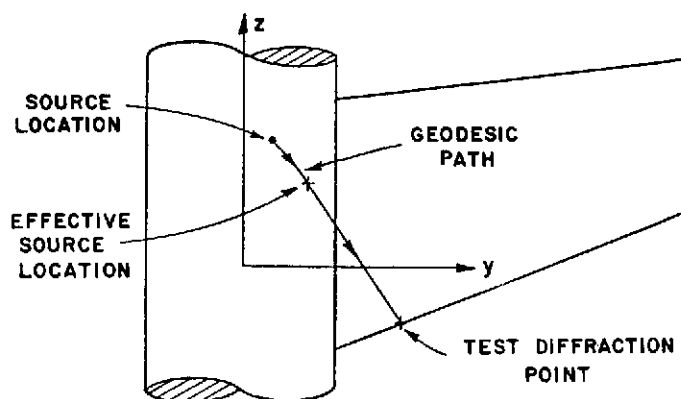
Fig. 9b. Diffraction problem in y-z plane.
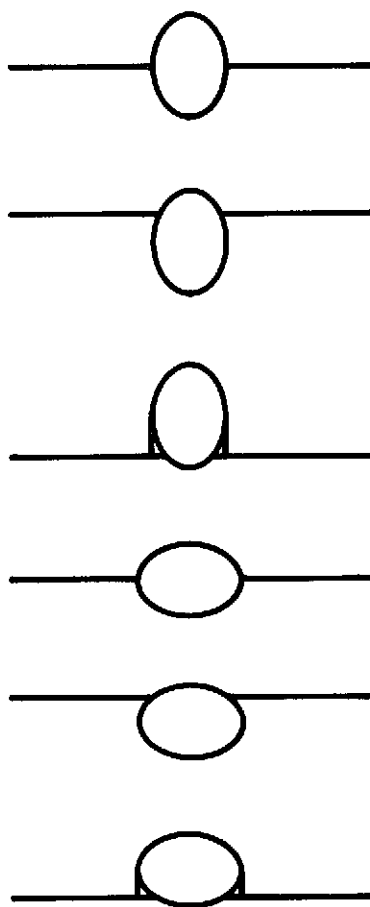
Fig. 10. Fuselage and wing geometry for theoretical aircraft model looking from the front.
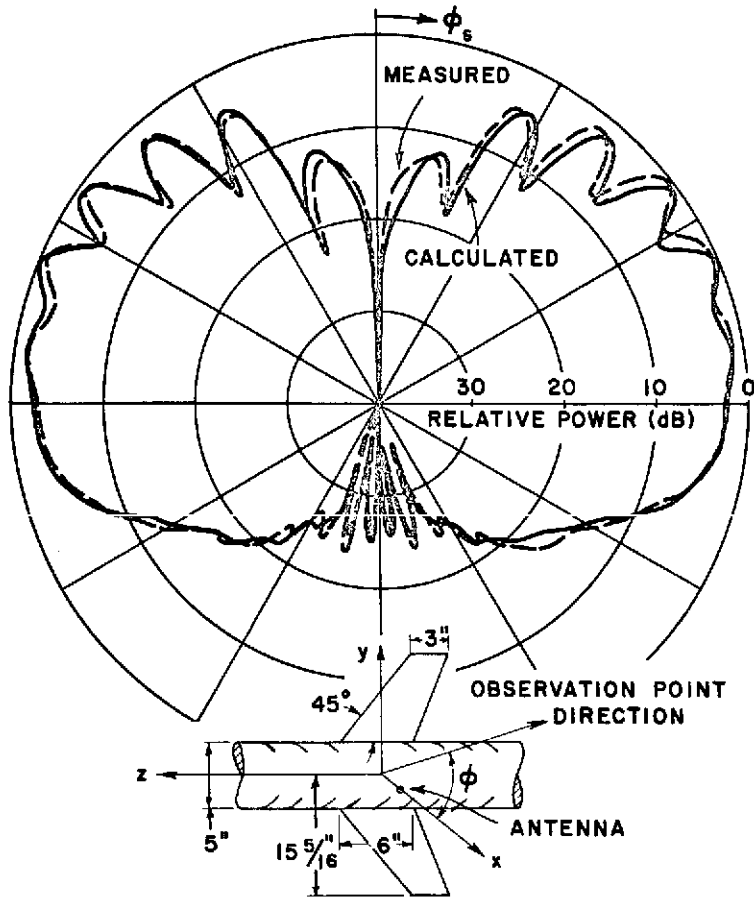
Fig. 11a. Roll plane pattern of monopole (E_ϕ) at f = 11.45 GHz.
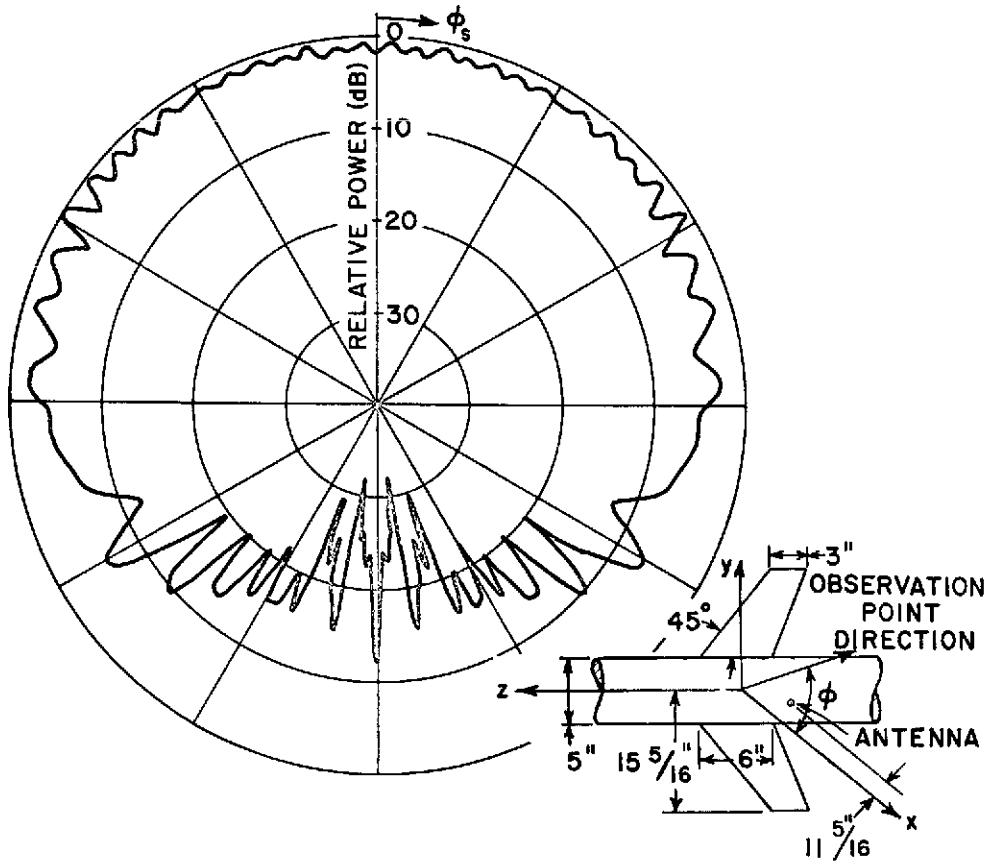
Fig. 11b. Roll plane pattern of axial slot (E_ϕ) at f = 11.45 GHz.
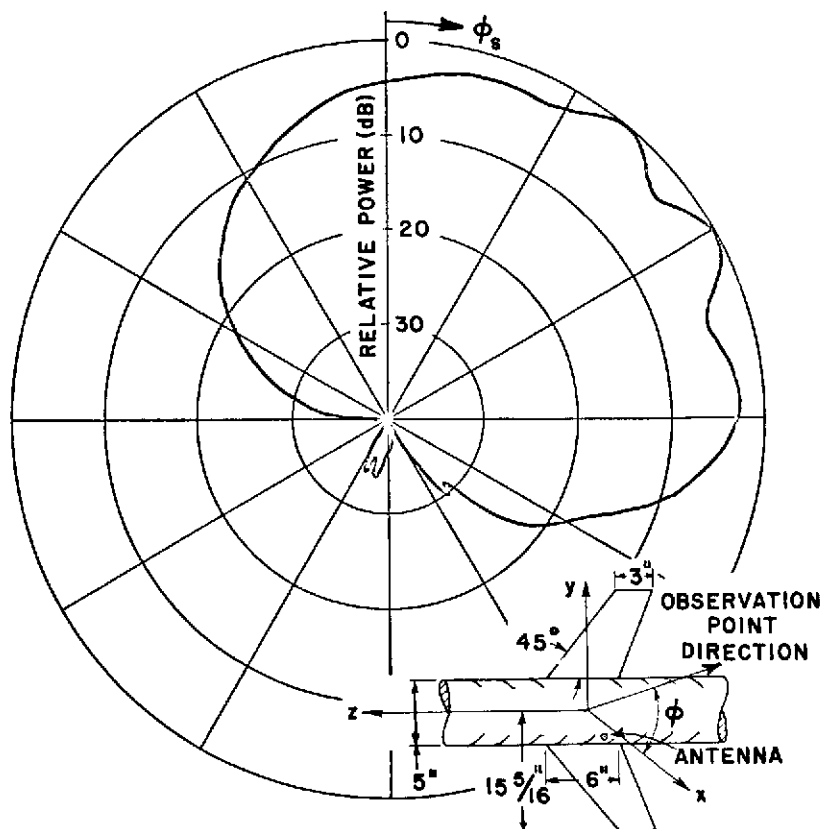
Fig. 11c. Roll plane pattern of a circumferential slot mounted over the wings but rotated 45° from the straight up direction of Fig. 11a.
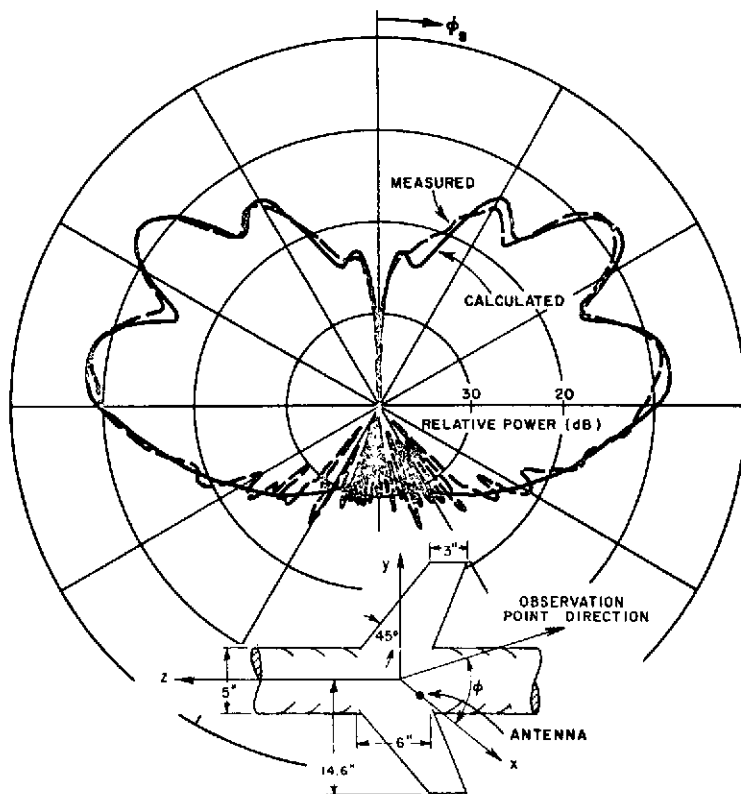
Fig. 12a. Roll plane pattern of a λ/4 monopole mounted on circular fuselage with wings attached at 45° above the central position.
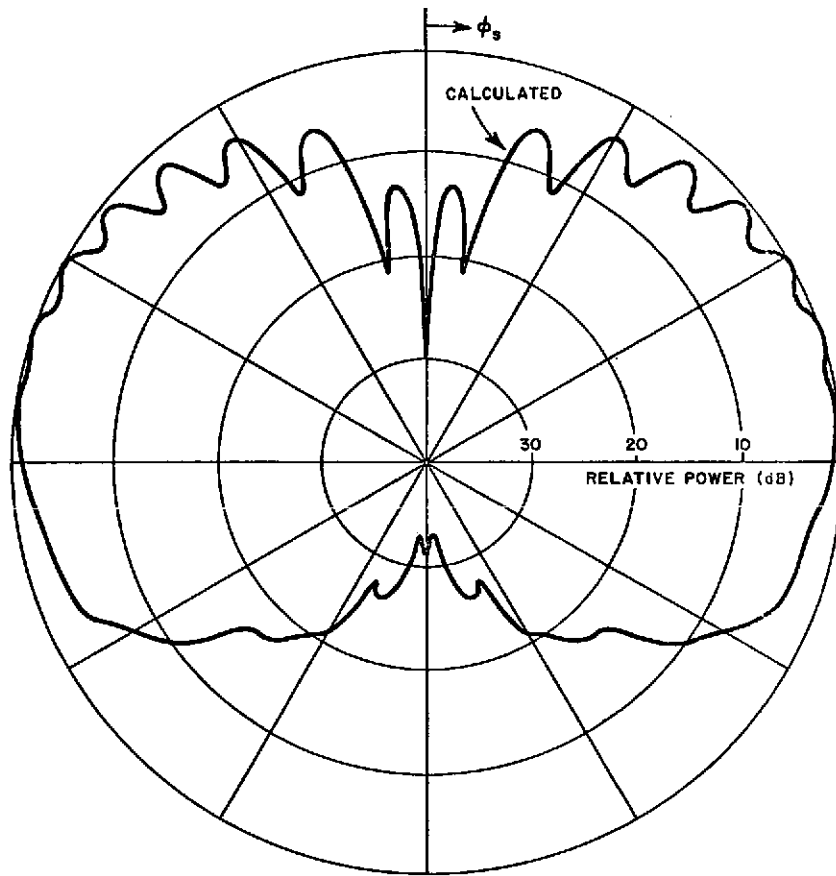
Fig. 12b. Roll plane pattern of a λ/4 monopole mounted on circular fuselage with wings attached at 45° below the central position, with same geometry as Fig. 12a otherwise.
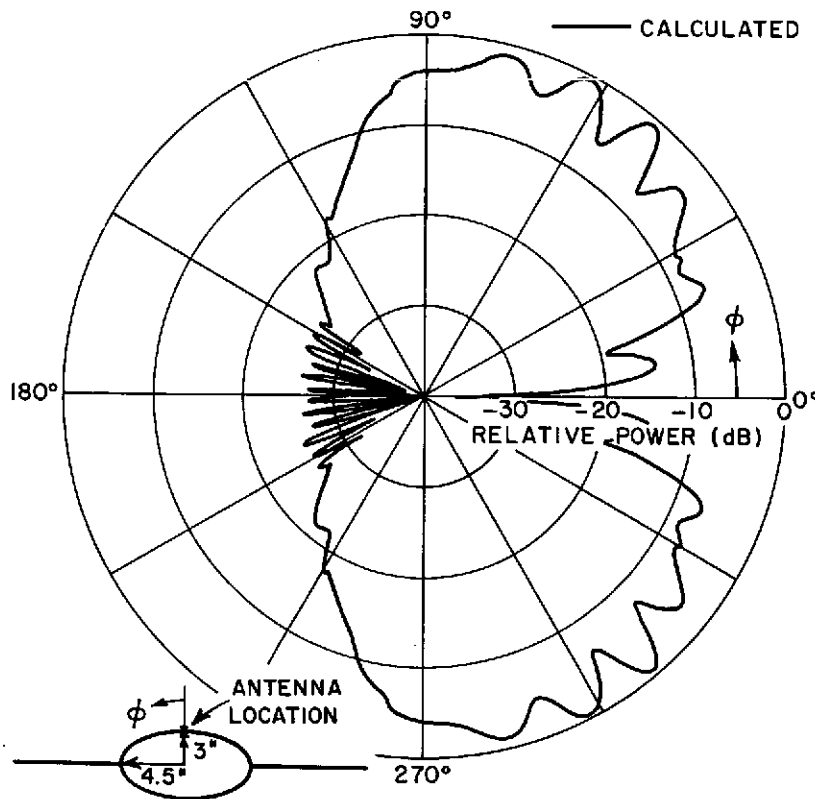
Fig. 13a. Roll plane pattern of a monopole mounted on an elliptic fuselage with centrally located wings at f = 8 GHz.
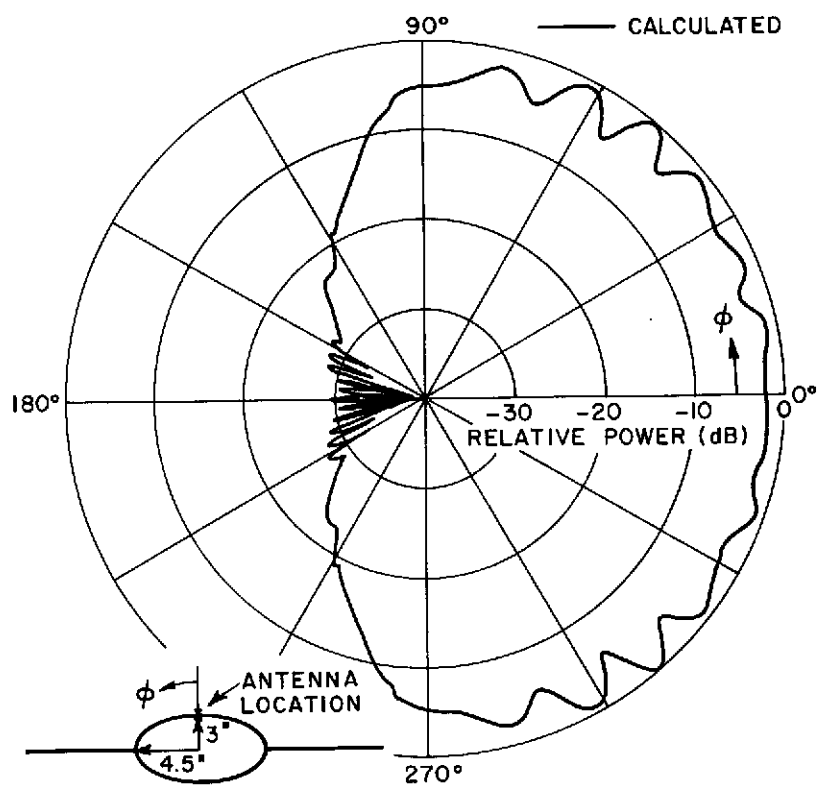
Fig. 13b. Roll plane pattern of an axial slot mounted on an elliptic fuselage with centrally located wings at f = 8 GHz.
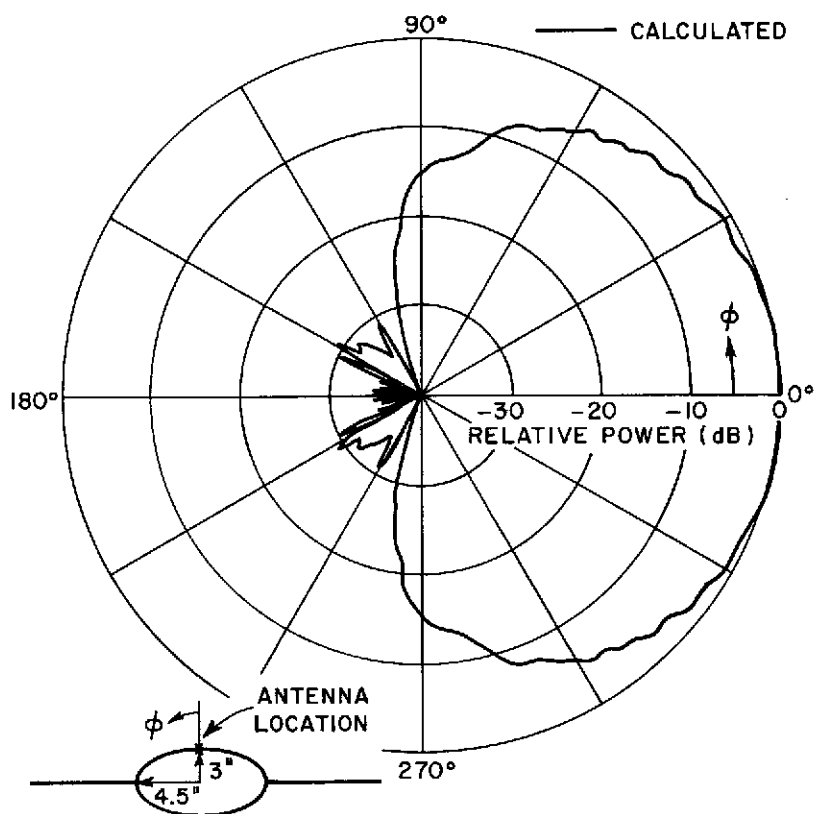
Fig. 13c. Roll plane pattern of a circumferential slot mounted on an elliptic fuselage with centrally located wings at f = 8 GHz.
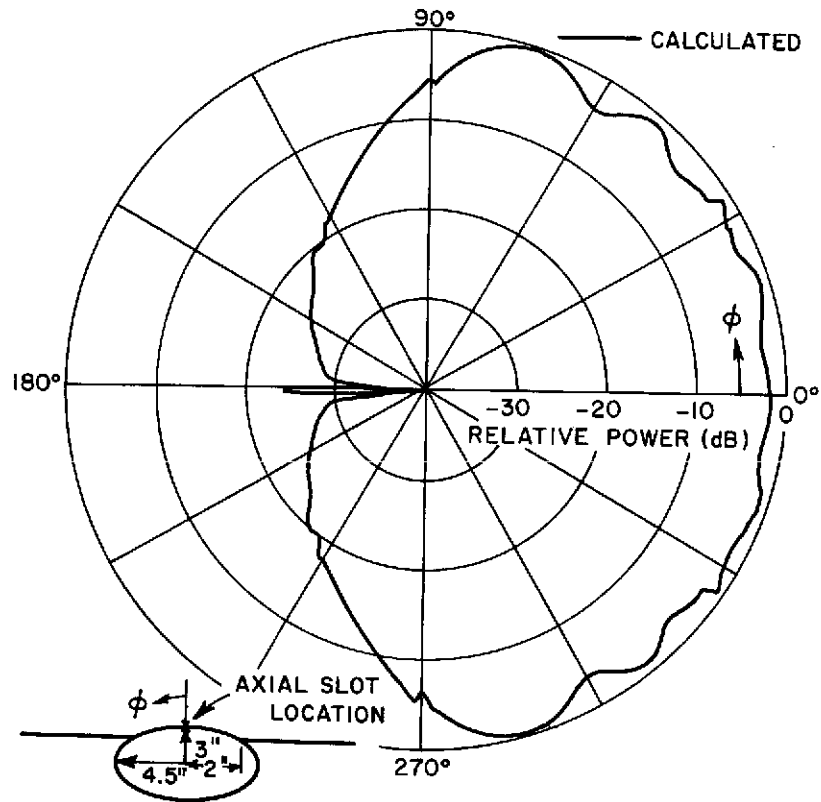
Fig. 14a. Roll plane pattern of an axial slot mounted on an elliptic
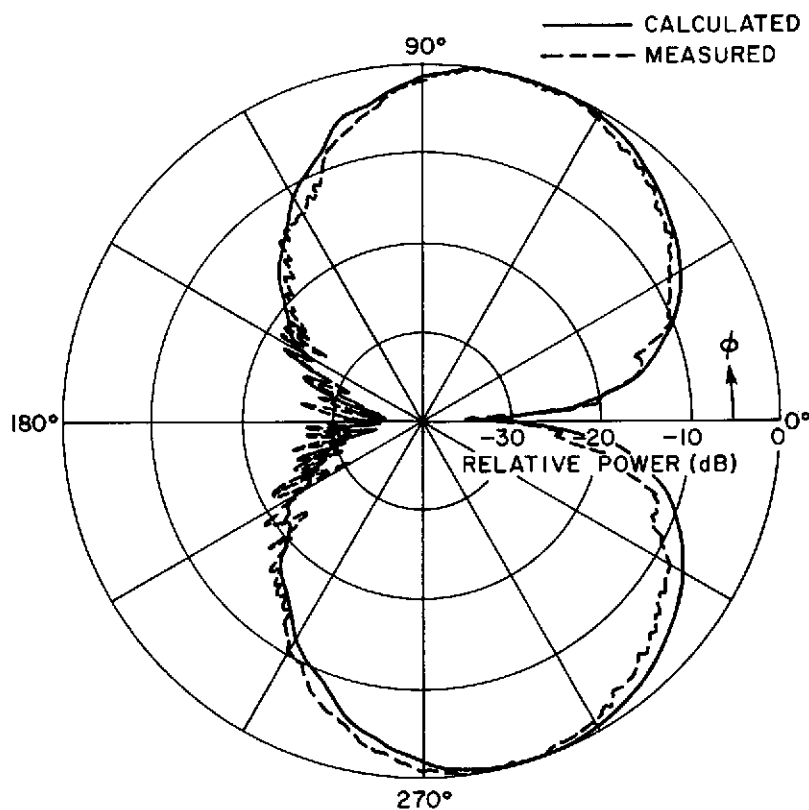fuselage with the wing attached above the central
location at f = 8 GHz.
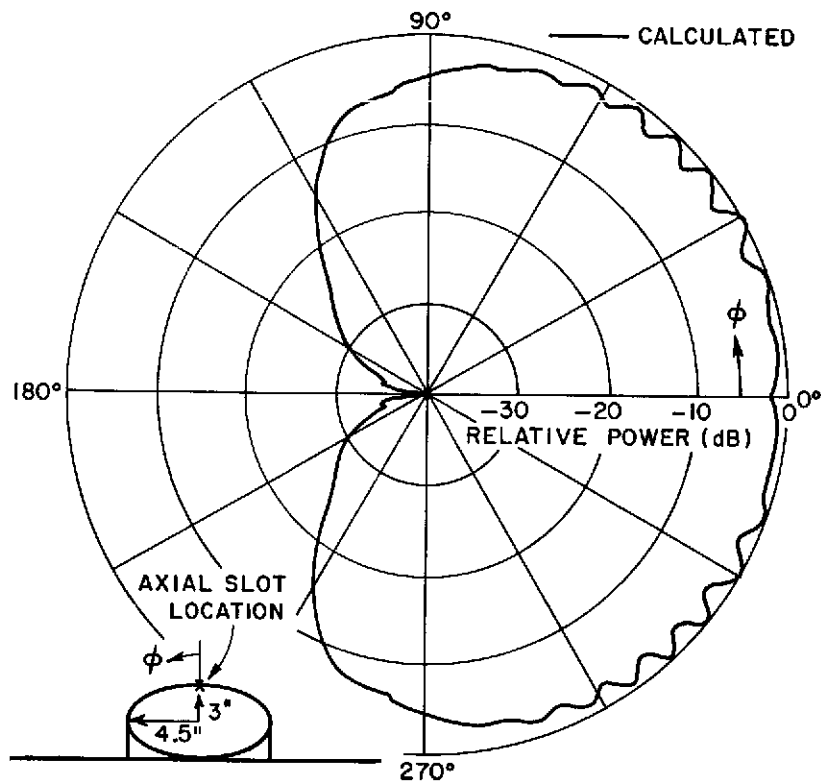
Fig. 14b. Roll plane pattern of an axial slot mounted on an elliptic
fuselage with the wings attached below the central
location at f = 8 GHz.

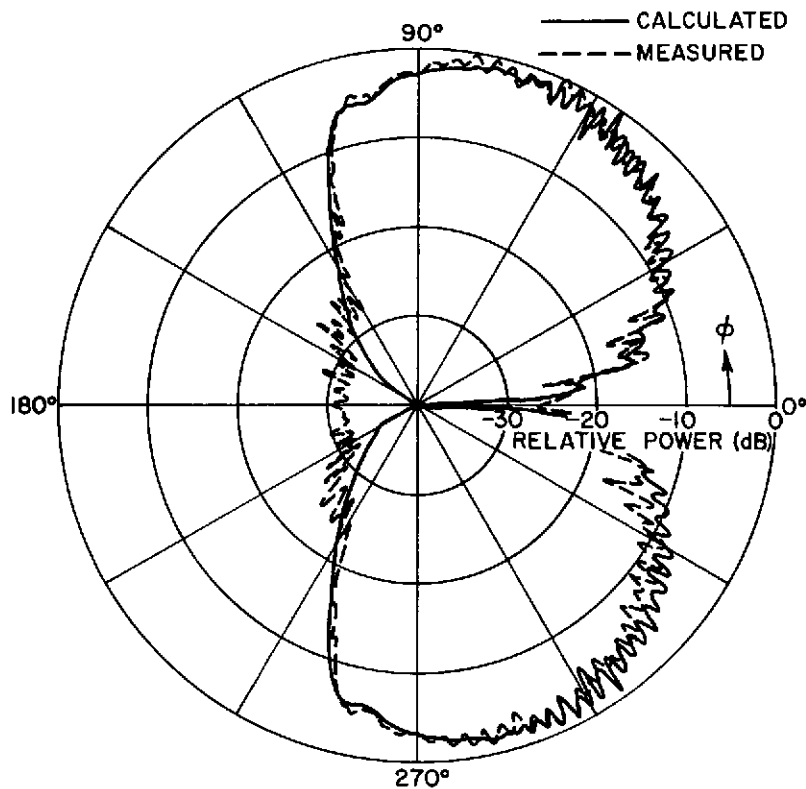Fig. 15a. A λ/4 monopole mounted on the fuselage of a KC-135 forward of the wings.

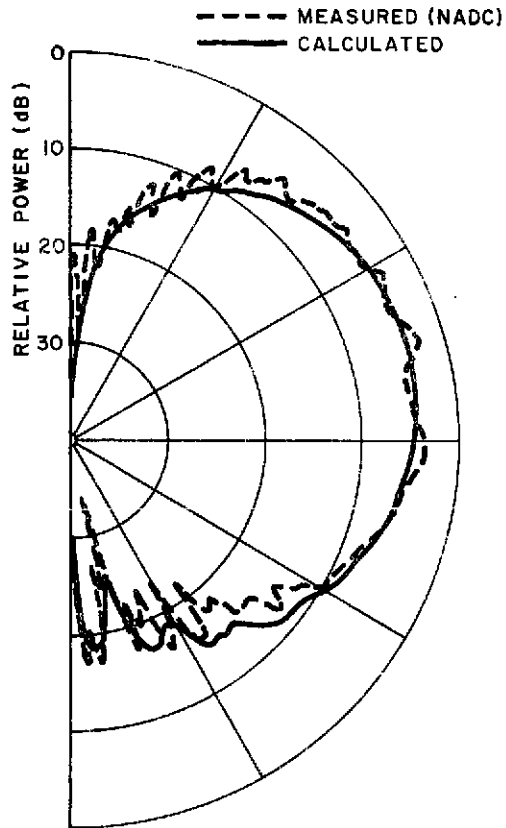Fig. 15b. A λ/4 monopole mounted on the fuselage of a KC-135 over the wings.

Fig. 16a. Roll plane pattern of a λ/4 monopole mounted 11" from the
nose on the bottom of an 1/8 scale model of an F-4
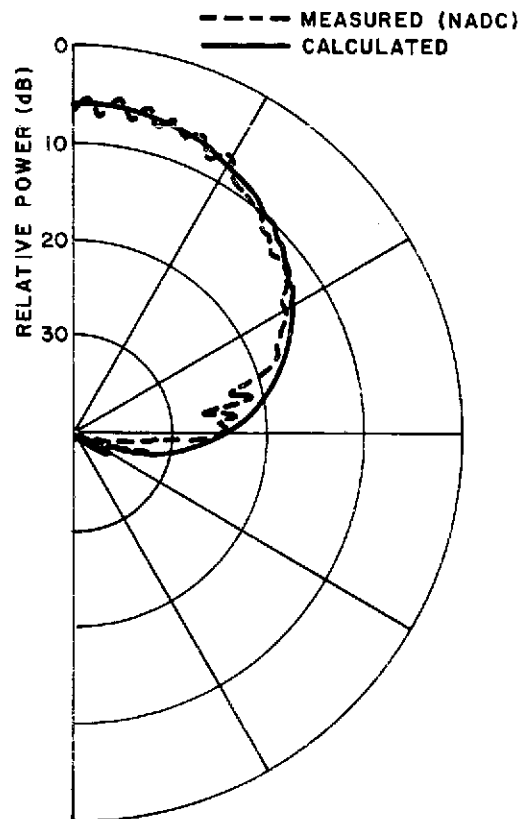aircraft at f = 8.0 GHz.

Fig. 16b. Roll pattern of a circumferential slot mounted 35-1/4"
from the nose on the top of an 1/8 scale model of an F-4
aircraft at f = 8.0 GHz.